

Stability analysis of wake-induced vibration of bluff bodies

W.YAO · R.K.JAIMAN

Received: date / Accepted: date

Abstract The wake-induced vibration (WIV) is highly nonlinear response characterised by large transverse force and vibration in the post-lock-in region or galloping type vibration. The recent finding [10,9] contributes the origin of WIV to the shifting stagnation point on the downstream cylinder or external unbalance rotating effects induced by Von Karmon like vortex shedding. Following our previous finding [14] in vortex induced vibration (VIV) mechanism, we report alternative explanation from linear stability perspective. We adopted reduced order modeling techniques to construct a linear representation of WIV system and perform corresponding linear stability analysis (LSA) . The fluid reduced order model (ROM) is constructed by using an eigensystem realization algorithm (ERA) and coupled with a transversely vibrating bluff body in a state space format. The results show that the WIV region and onset reduced velocity U_r can be predicted accurately by tracing the eigenvalue trajectories of the ROM for a range of U_r . The LSA reveals that it is the persisting unstable eigenvalue branch that sustains WIV. Therefore, this highly nonlinear behaviour has its linear origion. The sharp corner of square cylinder is found to have the stabilizing effects, therefore, the WIV onset U_r is larger than its circular cylinder counterpart. The work extends our previous understanding of the vortex induced vibration (VIV) lock-in mechanism to WIV at low Reynolds number and provides an expolation of the origion of WIV and why it persists at certain conditons.

Keywords Nonlinear · Wake-induced-vibration · Model reduction

1 Introduction

Vortex induced vibration (VIV) is a complex nonlinear coupling between the structure and the flow dynamic, which often results in large motion and reduce the

W.YAO
National University of Singapore, now at Queen's University Belfast
E-mail: w.yao@qub.ac.uk

R.K.JAIMAN
National University of Singapore

structural fatigue life. VIVs have broad interests in the fields of offshore, wind, aerospace and energy harvesting engineering due to its richness in fluid physics. In VIV lock-in regime, the vortex shedding frequency deviates from the Strouhal law and lock on to the structure natural frequency. This frequency lock-in phenomenon is typically characterized by high structure amplitude and therefore has been an active topic over the past decade ([11, 12, 3]).

The commonly accepted interpretation of VIVs is attributed to the classical resonance, which depends on vortex shedding frequency (f_{vs}) matching structure natural frequency (f_N). However, numerical simulation has shown that the peak amplitude arises in the vicinity of lock-in onset rather than at $f_{vs}/f_N \approx 1$. Recently, Yao and Jaiman [14] developed an efficient VIV reduced order model (ROM) using eigensystem realization algorithm (ERA) and successfully performed linear stability analysis (LSA) of VIV system. The authors show that the lock-in onset of bluff bodies is triggered by unstable structure mode (SM), and the low frequency galloping is characterized by persisting unstable SM. The understanding of lock-in mechanism by ERA-based ROM paves a way to develop a feedback control strategy for VIVs suppression [13].

The wake induced vibration or WIV is considered as the flow induced vibration in tandem configuration. The nature of VIV and WIV arises similarly from wake instability. However, WIV has its particular physics feature. Based on spacing to diameter ratio (L/D), the tandem cylinder is characterized by three interference regimes [10, 15, 6]: proximity interference ($1 \leq L/D \leq 1.2$ to 1.8), wake interference ($1.8 \leq L/D \leq 3.4$ to 3.8) and no interference ($L/D \geq 3.8$). In proximity regime, the vortex shedding from the upstream cylinder is suppressed and the tandem bodyies behave like a single bluff body, whereas the flow becomes intricate in wake interference and shear layer reattachment, intermittent vortex shedding, etc gradually appear as L/D increases. The no interference regime is dominated by the co-shedding, where vortex shedding occurs separately from both the cylinders.

The downstream cylinder experiences large response persisting to high reduced velocity which is typically defined as wake induced galloping [4]. Recent work [2] dissociates the WIV from galloping concept. The authors argue the WIV is sustained by unsteady vortex shedding that provides energy to the WIV system, and has different mechanism from VIV, which is considered as a *resonance* phenomenon. In another recent work [1], the authors provided a physical explanation for WIV by wake-stiffness concept. They argued that the wake-stiffness characterizes the WIV properties. The authors [2, 1] insists that the WIV is a non-resonance fluid induced vibration (FIV) with increasing amplitude beyond frequency lock-in regime, and is mainly due to unsteady wake.

R.C. Mysa et al.[10] investigated the origin of WIV at low Reynolds number ($Re, m^*, L = (100, 2.6, 5D)$). The authors contribute the large transverse vibration in the post-lock-in region to the continuous vorticity shed from the upstream cylinder impinging on the downstream. The interaction can in turn shift the stagnation point of downstream cylinder closer to low suction region and decrease the suction pressure compared to isolated cylinder, which leads to a larger transverse force and transverse vibration. Recently, Analogous to the linear force oscillator, the same authors [9] idealize the WIV system as a linear mass spring model with a periodic force and a rotation effects. The steady solution of the spring-mass with the rotation excitation does not decay for high frequency ratio ($f/f_N \gg 1$) or in the post-lock-in region. The aforementioned physical insight are concluded at

$Re > Re_{cr}$ or the unsteady vortex shedding commences. As shown in section 4.1, the large transverse vibration or galloping type response also appears at $Re < Re_{cr}$ or the flow is stable. Therefore, it is still worthwhile to exploring the origin of the WIV.

In our previous work for VIV linear stability analysis [14], we demonstrated that forward triangle cylinder galloping type response is sustained by persisting unstable eigenvalue branch of linear VIV system constructed by ERA method. In present work, we extend the physical insight to WIV by performing the linear stability analysis for WIV system. We will show in this paper that the WIV galloping type WIV response shares the same linear stability mechanism as forward triangle cylinder. Compared with circular cylinder, we show that the sharp corner of square cylinders also stabilize the WIV system or fluid-structure coupling in the sense that the WIV onset reduced velocity is postpone and the WIV amplitude is also reduced significantly. The paper is organized as follows. Section 2 introduces the FOM, ERA and ERA-based WIV ROM formulation in state space format. Section 3 describes the problem set-up. The LSA results are discussed in section 4 followed by conclusion in section 5.

2 Numerical methodology

2.1 Full-order model formulation

Consider the fluid domain $\Omega^f(t)$ with the spatial and temporal coordinates denoted by \mathbf{x}^f and t , respectively. The Navier-Stokes (NS) equations governing an incompressible flow in the ALE reference frame are

$$\rho^f \left(\frac{\partial \mathbf{u}^f}{\partial t} \Big|_\chi + (\mathbf{u}^f - \mathbf{w}) \cdot \nabla \mathbf{u}^f \right) = \nabla \cdot \boldsymbol{\sigma}^f + \mathbf{b}^f \text{ on } \Omega^f(t), \quad (1)$$

$$\nabla \cdot \mathbf{u}^f = 0 \text{ on } \Omega^f(t), \quad (2)$$

where ρ^f , \mathbf{u}^f , \mathbf{w} , $\boldsymbol{\sigma}^f$, and \mathbf{b}^f are the fluid density, the fluid velocity, the ALE mesh velocity, the Cauchy stress tensor and the body force per unit mass, respectively. For the partial time derivative in Eq. (1), the ALE referential coordinate χ is held fixed and for a Newtonian fluid $\boldsymbol{\sigma}^f$ is defined as

$$\boldsymbol{\sigma}^f = -p\mathbf{I} + \mu^f \left(\nabla \mathbf{u}^f + (\nabla \mathbf{u}^f)^T \right), \quad (3)$$

where p , μ^f and \mathbf{I} are the pressure, the dynamic viscosity of the fluid and an identity tensor, respectively. The ALE mesh nodes on the fluid domain $\Omega^f(\mathbf{x}^f, t)$ can be updated by solving a linear steady pseudo-elastic material model

$$\nabla \cdot \boldsymbol{\sigma}^m = \mathbf{0}, \quad (4)$$

$$\boldsymbol{\sigma}^m = (1 + k_m) \left[\left(\nabla \boldsymbol{\eta}^f + (\nabla \boldsymbol{\eta}^f)^T \right) + (\nabla \cdot \boldsymbol{\eta}^f) \mathbf{I} \right], \quad (5)$$

where $\boldsymbol{\sigma}^m$ is the stress experienced by the ALE mesh due to the strain induced by the rigid-body movement, $\boldsymbol{\eta}^f$ represents the ALE mesh node displacement and

k_m is a mesh stiffness variable chosen as a function of the element area to limit the distortion of small elements located in the immediate vicinity of the fluid-body interface. The WIV FOM or fluid-structure coupling is achieved through a partitioned staggered procedure [7,14].

Given a base flow \mathbf{u}_0 , the corresponding linearized NS equations can be written in a semi-discrete form as [13],

$$\mathbf{E} \frac{d\mathbf{Q}}{dt} = \mathbf{F}\mathbf{Q}, \quad (6)$$

where the matrices and vectors in Eq. (6) are

$$\mathbf{F} = \begin{pmatrix} -() \cdot \nabla \mathbf{u}_0 - \mathbf{u}_0 \cdot \nabla () + \mu (\nabla () + \nabla^T ()) & -\nabla () \\ \nabla \cdot () & \mathbf{0} \end{pmatrix}, \quad (7a)$$

$$\mathbf{G} = \begin{pmatrix} () \cdot \nabla \mathbf{u}_0 & \mathbf{0} \\ \mathbf{0} & \mathbf{0} \end{pmatrix}, \mathbf{E} = \begin{pmatrix} \mathbf{I} & \mathbf{0} \\ \mathbf{0} & \mathbf{0} \end{pmatrix}, \mathbf{Q} = \begin{pmatrix} \mathbf{u} \\ p \end{pmatrix}. \quad (7b)$$

The forward and adjoint modes can be derived by solving generalized eigenvalue problem of linearized NS equation Eq. (6), which can be written as $(\mathbf{A}_f + \sigma \mathbf{B}_f)\mathbf{p} = \mathbf{0}$, where the non-symmetric matrices \mathbf{A}_f and \mathbf{B}_f results from the spatial and temporal discretizations, σ denotes the eigenvalue of the discretized system, \mathbf{p} is the right eigenvectors (forward modes). The corresponding discrete adjoint problem can be obtained as $\mathbf{q}(\mathbf{A}_f + \sigma \mathbf{B}_f) = \mathbf{0}$, where \mathbf{q} is the left eigenvector of the discrete system and represents the approximation of the adjoint modes [5].

2.2 ERA-based model reduction

The linear time-invariant (LTI) and multiple-input multiple-output (MIMO) model represented in a state-space form at discrete times $t = k\Delta t$, $k = 0, 1, 2, \dots$, with a constant sampling time Δt reads

$$\left. \begin{array}{l} \mathbf{x}_r(k+1) = \mathbf{A}_r \mathbf{x}_r(k) + \mathbf{B}_r \mathbf{u}(k) \\ \mathbf{y}_r(k) = \mathbf{C}_r \mathbf{x}_r(k) + \mathbf{D}_r \mathbf{u}(k) \end{array} \right\}, \quad (8)$$

where \mathbf{x}_r is an n_r -dimensional state vector, \mathbf{u} denotes a q -dimensional input vector and \mathbf{y}_r is a p -dimensional output vector. The system matrices are $(\mathbf{A}_r, \mathbf{B}_r, \mathbf{C}_r, \mathbf{D}_r)$ and derived from ERA method [8]. To construct the ERA-based ROM, the impulse response of NS equation is first defined as \mathbf{y} , based on which the generalized block Hankel matrix $r \times s$ can be constructed as

$$\mathbf{H}(k-1) = \begin{bmatrix} \mathbf{y}_{k+1} & \mathbf{y}_{k+2} & \cdots & \mathbf{y}_{k+s} \\ \mathbf{y}_{k+2} & \mathbf{y}_{k+3} & \cdots & \mathbf{y}_{k+s+1} \\ \vdots & \vdots & \ddots & \vdots \\ \mathbf{y}_{k+r} & \mathbf{y}_{k+r+1} & \cdots & \mathbf{y}_{k+(s+r-1)} \end{bmatrix}, \quad (9)$$

and by applying singular value decomposition (SVD) of Hankel matrix $\mathbf{H}(0)$ as

$$\mathbf{H}(0) = \mathbf{U} \Sigma \mathbf{V}^* = [\mathbf{U}_1 \quad \mathbf{U}_2] \begin{bmatrix} \Sigma_1 & \mathbf{0} \\ \mathbf{0} & \Sigma_2 \end{bmatrix} \begin{bmatrix} \mathbf{V}_1^* \\ \mathbf{V}_2^* \end{bmatrix} \quad (10)$$

where the diagonal matrix Σ are the Hankel singular values (HSVs). The block matrix Σ_2 contains the zeros or negligible elements. By truncating the dynamically less significant states, we estimate $\mathbf{H}(0) \approx \mathbf{U}_1 \Sigma_1 \mathbf{V}_1^*$. The state space matrices ($\mathbf{A}_r, \mathbf{B}_r, \mathbf{C}_r, \mathbf{D}_r$) are obtained by

$$\left. \begin{array}{l} \mathbf{A}_r = \Sigma_1^{-1/2} \mathbf{U}_1^* \mathbf{H}(1) \mathbf{V}_1 \Sigma_1^{-1/2} \\ \mathbf{B}_r = \Sigma_1^{1/2} \mathbf{V}_1^* \mathbf{E}_m \\ \mathbf{C}_r = \mathbf{E}_t^* \mathbf{U}_1 \Sigma_1^{1/2} \\ \mathbf{D}_r = \mathbf{y}_1 \end{array} \right\} \quad (11)$$

Here, $\mathbf{E}_m^* = [\mathbf{I}_q \quad \mathbf{0}]_{q \times N}$, $\mathbf{E}_t^* = [\mathbf{I}_p \quad \mathbf{0}]_{p \times M}$, where $N = s \times q$, $M = r \times p$, and $\mathbf{I}_{p,q}$ are the identity matrices.

2.3 Reduced order model for WIV

In the present work, we only consider the transverse motion of cylinder for the sake of simplicity [14]. The structural governing equations can be expressed as,

$$\ddot{Y} + 4\zeta\pi F_s \dot{Y} + (2\pi F_s)^2 Y = \frac{a_s}{m^*} C_l, \quad (12)$$

where Y is the transverse displacement; C_l is the lift coefficient, m^* and ζ are the ratio of the mass of the vibrating structure to the mass of the displaced fluid and the damping coefficient, respectively; F_s is the reduced natural frequency of the structure defined as $F_s = f_N D/U = 1/U_r$, where U_r is the reduced velocity. $a_s = \frac{2}{\pi}$ for a circular cylinder, and $a_s = 0.5$ for a square cylinder. Equation (12) can be casted into space format as,

$$\dot{\mathbf{x}}_s = \mathbf{A}_s \mathbf{x}_s + \mathbf{B}_s C_l, \quad (13)$$

where the state matrices and vectors are

$$\mathbf{A}_s = \begin{bmatrix} 0 & 1 \\ -(2\pi F_s)^2 & -4\zeta\pi F_s \end{bmatrix}, \quad \mathbf{B}_s = \begin{bmatrix} 0 \\ \frac{a_s}{m^*} \end{bmatrix}, \quad \mathbf{x}_s = \begin{bmatrix} Y \\ \dot{Y} \end{bmatrix}.$$

The resultant fluid and structure coupled system ROM is formulated as,

$$\mathbf{x}_{fs}(k+1) = \begin{bmatrix} \mathbf{A}_{sd} + \mathbf{B}_{sd} \mathbf{D}_r \mathbf{C}_{sd} & \mathbf{B}_{sd} \mathbf{C}_r \\ \mathbf{B}_r \mathbf{C}_{sd} & \mathbf{A}_r \end{bmatrix} \mathbf{x}_{fs}(k) = \mathbf{A}_{fs} \mathbf{x}_{fs}(k), \quad (14)$$

where $\mathbf{A}_{sd} = e^{\mathbf{A}_s \Delta t}$, $\mathbf{B}_{sd} = \mathbf{A}_s^{-1} (e^{\mathbf{A}_s \Delta t} - \mathbf{I}) \mathbf{B}_s$.

3 Numerical set-up and verification

3.1 Problem definition

Similar to [14], figure 1 shows a schematic diagram of the setup used for WIV linear stability analysis. The coordinate origin is located at the center of the two bluff bodies. The streamwise and transverse directions are denoted x and y , respectively. A stream of incompressible fluid enters into the domain from an inlet boundary Γ_{in}

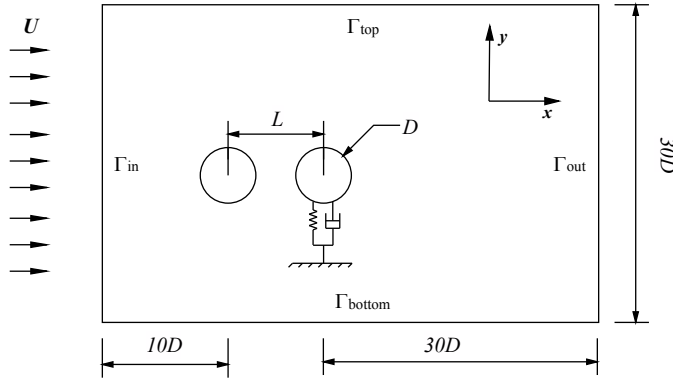


Fig. 1: Schematic diagram of a representative bluff body of elastically mounted cylinder in the wake of stationary cylinder. Computational domain and boundary conditions are shown.

at a horizontal velocity $(u, v) = (U, 0)$, where u and v denote the streamwise and transverse velocities, respectively. The downstream bluff body with mass m and characteristic diameter D is mounted on a linear spring in the transverse direction. The damping coefficient ζ is set to zero in the present work. The domain size is similarly set up as [14]. No-slip wall condition is implemented on the surfaces of the bluff body, and a traction-free boundary condition is implemented along the outlet Γ_{out} while the slip wall condition is implemented on the top Γ_{top} and bottom Γ_{bottom} boundaries. All length scales are normalized by the characteristic dimension D , velocities with the free stream velocity U , and frequencies with U/D . The Reynolds number Re of flow is based on the characteristic dimension D , kinematic viscosity of fluid and free-stream speed U . According to the mesh convergence study in [14], we consider the mesh consisting of 20912 $\mathbb{P}_2/\mathbb{P}_1$ isoparametric elements is sufficient for current WIV LSA study. The mesh is shown in figure 2 and the corresponding central rectangle represents the fine mesh region around the cylinder bodies. The mesh in the cylinder wake is appropriately refined to resolve the alternate vortex shedding.

3.2 Linear stability analysis of stationary tandem cylinder

At $(Re, L) = (60, 2D)$, the WIV ERA-based ROM is first constructed for circular cylinder tandem configuration. The based flow, as shown in the figure 3, is computed via fixed point iteration without the time dependent term in the NS equation. Following the ERA-based ROM construction procedure in [14], 1000 impulse outputs (C_l) are stacked by imposing $\delta(t) = 10^{-4}$ on the transverse displacement Y of downstream cylinder with time step size $\Delta t = 0.05$. Subsequently, 25th ROM is determined by examining the decaying singular value of Hankel matrix [8]. A good match between FOM and 25th ROM is found in figure 4(b). The FOM results are derived by solving a generalized eigenvalue problem of Eq. (6). The impulse response gradually diverges at $Re = 120$ and indicates that real part of the least damped eigenvalue is positive and the uncoupled fluid system is un-

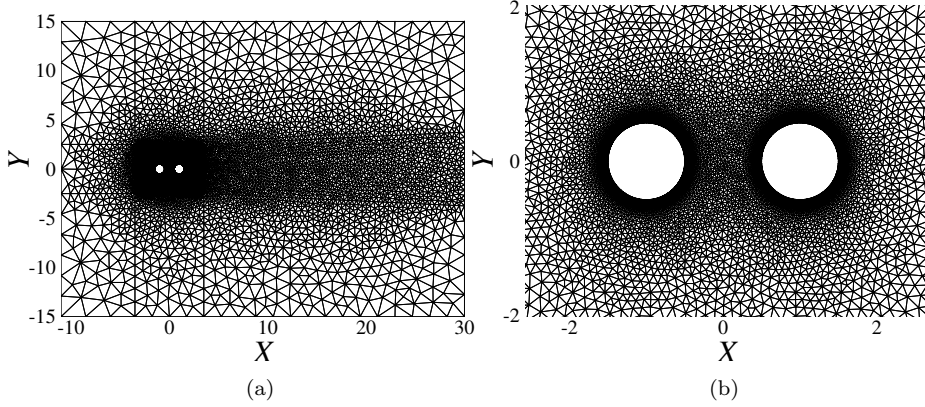


Fig. 2: Finite element mesh with $\mathbb{P}_2/\mathbb{P}_1$ discretization: (a) full domain discretization and (b) close-up view of in the vicinity of the tandem cylinder.

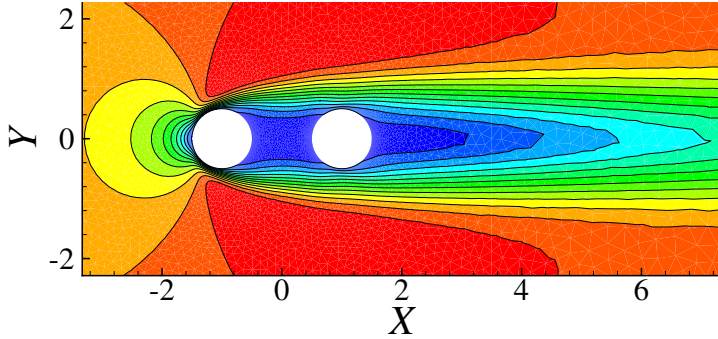


Fig. 3: Base flow of tandem circular cylinder at $(Re, L) = (60, 2D)$; The streamwise velocity contours are shown. The contour levels are from -0.1 to 1.2 in increments of 0.1.

stable. On the other hand, the decaying impulse response is observed for $Re = 60$ and indicates the stable fluid system. The least damped eigenvalue predicted by ERA-based ROM is compared with FOM in figure 5. It is evident that the flow becomes unstable when $Re_{cr} \approx 90$ or the real part of the least damped eigenvalue approaches zero.

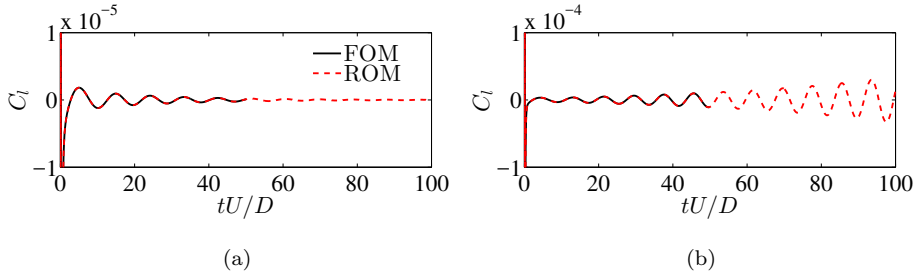


Fig. 4: The lift coefficient history of the 25th ROM compared with FOM subject to the impulse response. (a) $Re = 60$. (b) $Re = 120$.

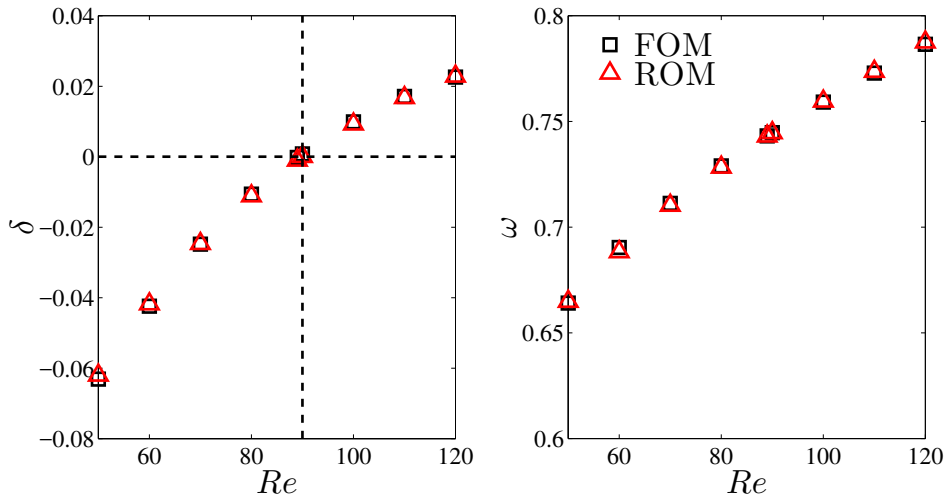


Fig. 5: The growth rate and frequency of the least damped eigenvalue for the flow past a tandem circular cylinder with $L = 2D$: (a) growth rate σ and (b) frequency ω . The cylinder wake becomes unstable when the growth rate crosses $\sigma = 0$ line at the critical $Re_{cr} \approx 90$ and the vortex shedding emanates.

4 Results and discussion

4.1 WIV of circular cylinder

Figure 6 shows the root loci of the WIV ERA-based ROM as a function of reduced velocity U_r with $2 \leq U_r \leq 40$. Following previous work in [14], the terminology WMI and WMII are adopted to classify the eigenvalue branches. As can be seen, the WMII branch arises from the high frequency region or the top of the complex plane, while the WMI branch originates from the uncoupled mode and travels down to the low frequency or bottom of the complex plane. As elucidated in the

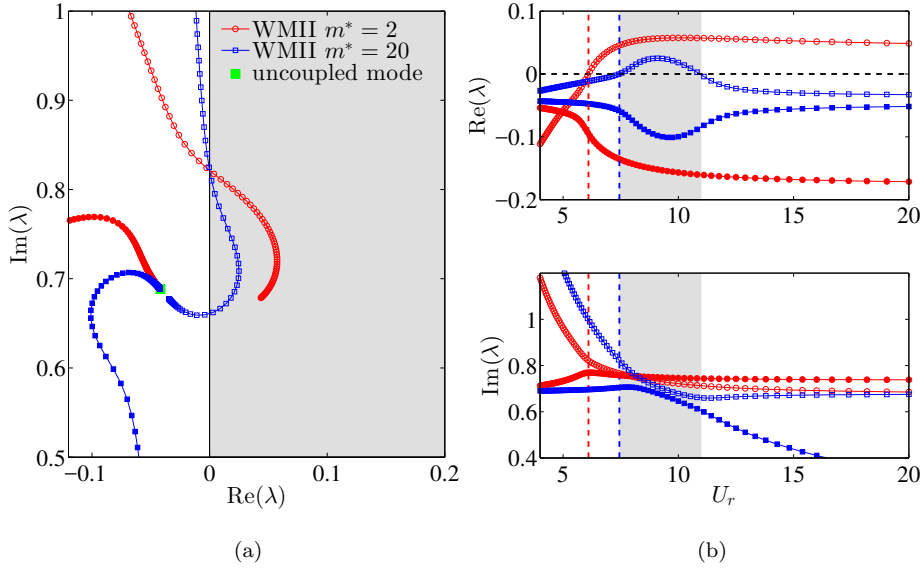


Fig. 6: Eigenspectrum of the ERA-based ROM at $(Re, L) = (60, 2D)$: (a) root loci as a function of the reduced velocity U_r , where the unstable right-half ($\text{Re}(\lambda) > 0$) plane is shaded in grey color. The WMI is denoted by filled symbols with the same shape as those for the WMII. The uncoupled wake mode $\lambda = -0.042 + 0.69i$. (b) Real and imaginary parts of the root loci at $(Re, L) = (60, 2D)$. The WIV region at $m^* = 20$ is shaded in grey colour, which is defined by $7.44 \leq U_r \leq 11.0$. - - - and - - - - represent WIV onset $U_r \approx 6.1$ and $U_r \approx 7.44$ for $m^* = (2, 20)$, respectively.

figure 6, the real part of WMII branch remains unstable when $U_r \geq 6.1$ and WMI branch is stable, which indicates the WIV persists at $m^* = 2$. The finding is further confirmed by the FOM in figure 7, where the WIV onset $U_r = 5.9$ and the WIV remains for $U_r \geq 5.9$. Figure 6 shows that the WMI branch is only unstable when $7.44 \leq U_r \leq 11.0$ at $m^* = 20$, which is evident from the figure 7. Furthermore, in figure 6(b) (bottom), the $\text{Im}(\lambda)$ plot shows the characteristic anticrossing between WMI and WMII for the low mass ratio $m^* = 2$. This intrinsic property of strong coupling system is also found for single cylinder VIV system at low mass ration [14]. The two counter-rotating vortices (2S mode) are released at onset $U_r = 5.9$ and $(Re, m^*, L) = (60, 2, 2D)$ as shown in figure 8. The figure 9 and 10 depict the transverse displacement and lift traces with the corresponding spectrum, which confirms the high harmonid response of WIV.

Apart from the unstable eigenvalue branches, it is also interesting to see the WIV from the engery transfer viewpoint. The engery transfer over one period T for WIV system is derived as equation 17 in Appendix A. The E_c is defined by excluding the exponential growth/decay rate. The figure 11 suggests that energy source to sustain the WIV is the unstable WMII at $(Re, L) = (60, 2D)$.

As shown 12, the uncoupled mode moves to the right half-complex-plane at $Re = 100$. Compared with root loci at $Re = 60$, figure 12 shows that the eigenvalue branches moves to high frequency regime or upper part of complex plane. The onset

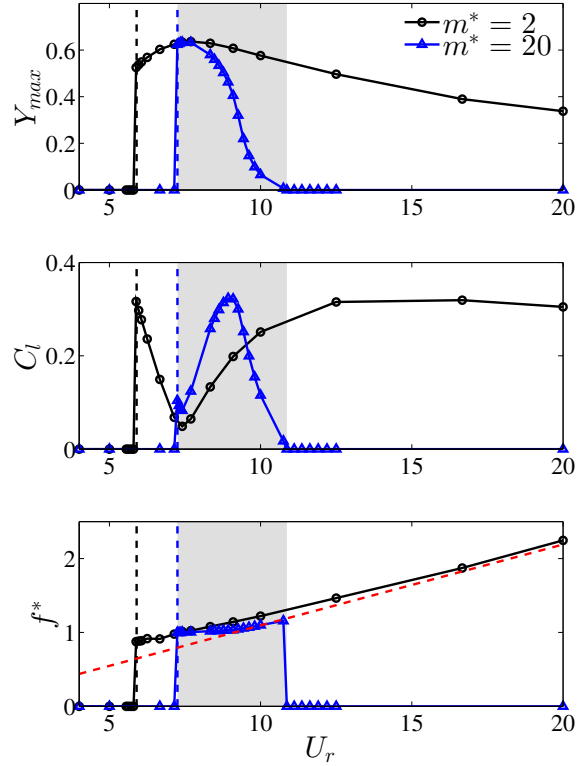


Fig. 7: Normalized maximum amplitude Y_{max} and rms value of lift coefficient C_l as a function of reduced velocity U_r at $(L, Re) = (2D, 60)$. The WIV region $7.25 \leq U_r \leq 10.87$ at $m^* = 20$ is shaded in grey colour. - - - and - - - - represent WIV onset $U_r = 5.9$ and $U_r = 7.25$, respectively. - - - is the uncoupled mode frequency predicted by ROM.

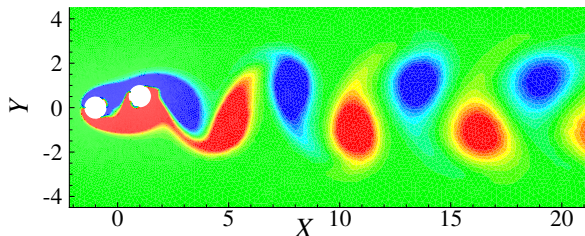


Fig. 8: Instantaneous vorticity contours of WIV onset ($U_r = 7.25$) at $(Re, m^*, L) = (60, 2, 2D)$. The contour levels are from 0.5 to 0.5 in increments of 0.067 and the flow is from left to right.

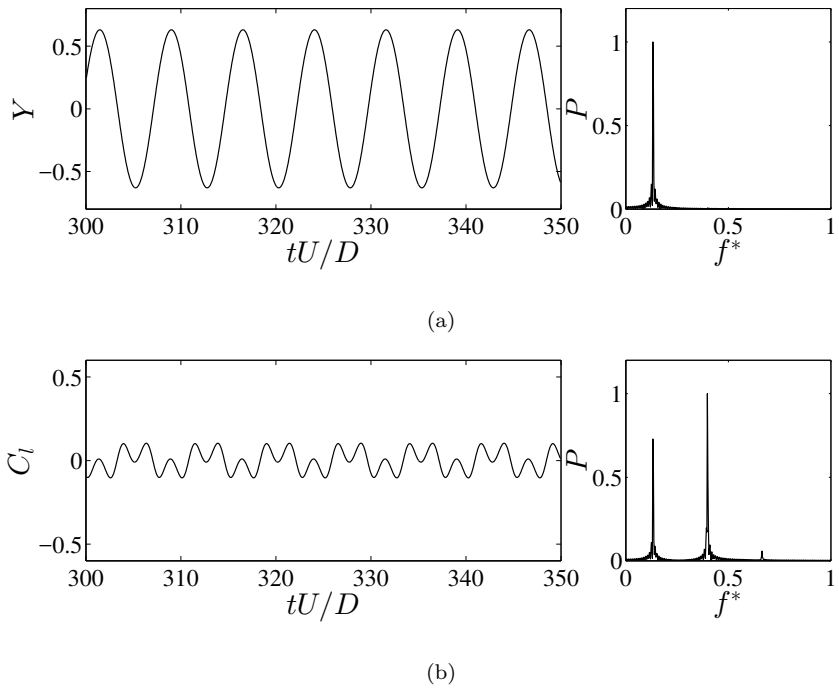


Fig. 9: FOM results of circular WIV at $(Re, m^*, L) = (60, 2, 2D)$: temporal variation of (a) transverse amplitude, and (b) lift coefficient; normalized power spectrum P versus f^* of: (a) transverse amplitude, (b) lift coefficient at reduced velocity $U_r \approx 7.69$ or $F_s = 0.13$, where $f^* = f/F_s$ is the frequency of lift and transverse displacement normalized by reduced natural frequency F_s . A third-harmonic frequency is evident in C_l .

U_r of WIV predicted by ERA-based ROM is at $U_r \approx 5.4$. Figure 17 shows the instantaneous vortex structure at onset reduced velocity $U_r \approx 5.3$ which shows C(2S) pattern.

4.2 WIV of square cylinder

In this section, we further explore the WIV of square cylinder. In our previous work [14], we demonstrate that the sharp corner has stabilizing effects for fluid structure coupling. Thereofre, It is interesting to investigate the WIV mechanism of square cylinder by means of ERA-based ROM. The flow region with high sensitivity and strong response or wavemaker region is determined by computing the pointwise product of the forward and adjoint global modes [5]. Figure 14 shows that the wavemaker region of the circular tandem cylinder has higher value and moves closer to the cylinders than its circular counterpart, which suggests that the circular tandem cylinder has stronger fluid and structure interation level.

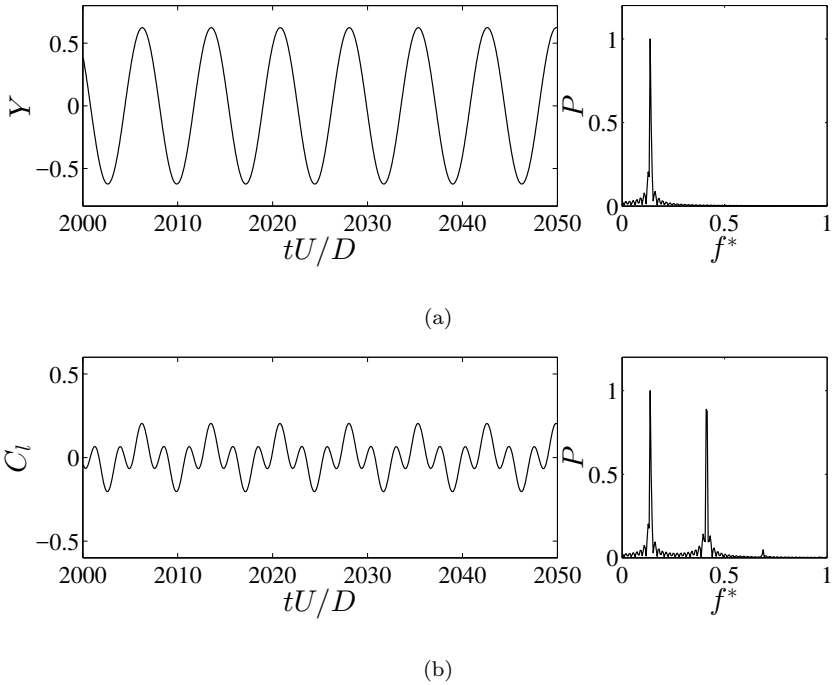


Fig. 10: FOM results of circular WIV at $(Re, m^*, L) = (60, 20, 2D)$: temporal variation of (a) transverse amplitude, and (b) lift coefficient; normalized power spectrum P versus f^* of: (a) transverse amplitude, (b) lift coefficient at onset reduced velocity $U_r \approx 7.25$ or $F_s = 0.138$, where $f^* = f/F_s$ is the frequency of lift and transverse displacement normalized by reduced natural frequency F_s . A third-harmonic frequency is evident in C_l .

5 Concluding remarks

WIV is a highly nonlinear response characterized by high amplitude in post-lock-in region. In this study, we adopted ERA-based model reduction to investigate the origin of WIV phenomena. The ERA-based ROM only relies on the impulse response of the NS equations and is efficient for linear stability analysis (LSA) of nonlinear fluid and structure coupling system. The LSA reveals that the persisting unstable eigenvalue branch sustains the WIV in the post-lock-in region. The results also show that the WIV can persist even at $Re < Re_{cr}$, whereas the authors in [10, 9] only consider the unsteady vortex shed from the upstream cylinder impinging on the downstream cylinder as the origin of this nonlinear behavior. The analysis of square cylinder shows that the sharp corner has the stabilizing effect for fluid and structure interaction in the sense that onset reduced velocity is postponed and amplitude is reduced significantly. WIV is a nonlinear response, however, the work suggests that it has the linear origin. Hence, LSA analysis lays a foundation to develop feedback control strategy to stabilize the WIV system by shifting the unstable eigenvalues to left-complex-half plane.

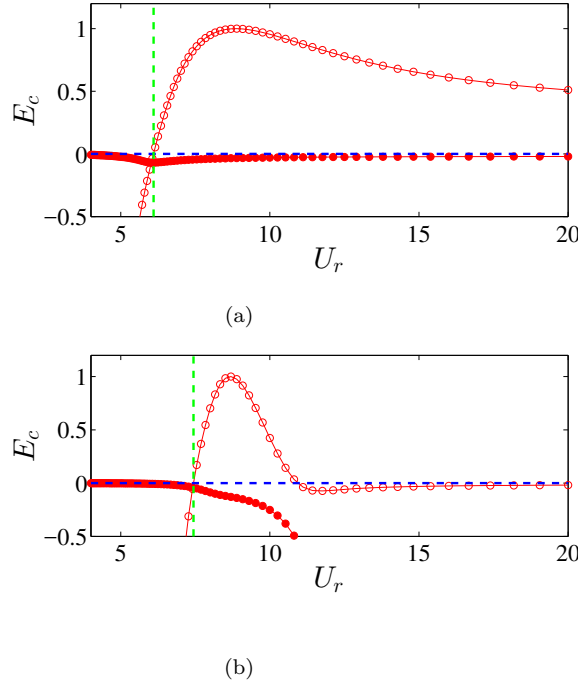


Fig. 11: E_c as a function of reduced velocity U_r at $(L, Re) = (2D, 60)$. (a) $m^* = 2$, and (b) $m^* = 20$. --- represents the onset reduced velocity U_r .

Appendix A: Energy Transfer for WIV

Following our previous work on VIV [14], the displacement and lift coefficient can be obtained for the WIV linear system as,

$$\left. \begin{aligned} Y &= \hat{Y} e^{\lambda_r t} \cos(\lambda_i t) \\ C_l &= \hat{C}_l e^{\lambda_r t} \cos(\lambda_i t + \phi) \end{aligned} \right\}, \quad (15)$$

where $\lambda = \lambda_r + i\lambda_i$ is eigenvalue with real λ_r and imaginary λ_i components, \hat{Y} and \hat{C}_l denote the magnitudes of eigenmodes. The phase angle difference is derived by plugging the Eq. (15) into Eq. (12), and refer to [14] for details.

$$\sin \phi = \frac{2\lambda_r \lambda_i}{\sqrt{(\lambda_r^2 + (2\pi F_s)^2 + \lambda_i^2)^2 - (4\pi \lambda_i F_s)^2}}. \quad (16)$$

The energy transfer per cycle is defined as,

$$\begin{aligned} E(t) &= \int_t^{t+\frac{2\pi}{\lambda_i}} \dot{Y} \hat{C}_l dt \\ &= \frac{1}{2} (\lambda_i \sin(\phi) + \lambda_r \cos(\phi) + \lambda_r \cos(2\lambda_i t + \phi)) \int_t^{t+\frac{2\pi}{\lambda_i}} e^{2\lambda_r t} dt \end{aligned} \quad (17)$$

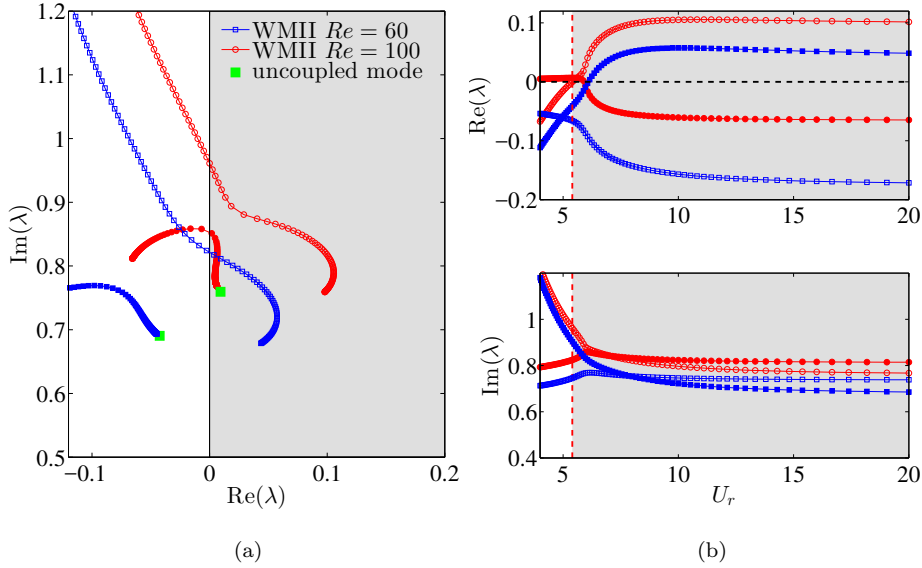


Fig. 12: Eigenspectrum of the ERA-based ROM at $(m^*, L) = (2, 2D)$: (a) root loci as a function of the reduced velocity U_r , where the unstable right-half ($\text{Re}(\lambda) > 0$) plane is shaded in grey color. The WMI is denoted by filled symbols with the same shape as those for the WMII. The uncoupled wake mode $\lambda = 0.01 + 0.759i$. (b) Real and imaginary parts of the root loci at $(Re, L) = (100, 2D)$. The WIV region at $(Re, m^*) = (100, 2)$ is shaded in grey colour, which is defined by $U_r \geq 5.4$.

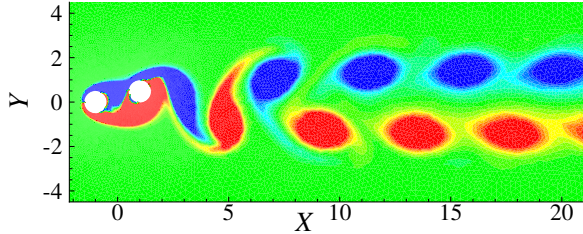


Fig. 13: Instantaneous vorticity contours of WIV onset ($U_r = 5.3$) at $(Re, m^*, L) = (100, 2, 2D)$. The contour levels are from 0.5 to 0.5 in increments of 0.067 and the flow is from left to right.

E_c is defined by excluding the exponential growth/decay rate λ_r in Eq. (17),

$$E_c = \pi \hat{Y} \hat{C}_l \sin(\phi) \quad (18)$$

References

- Assi, G.R.S., Bearman, P.W., Carmo, B.S., Meneghini, J.R., Sherwin, S.J., Willden, R.H.J.: The role of wake stiffness on the wake-induced vibration of the downstream

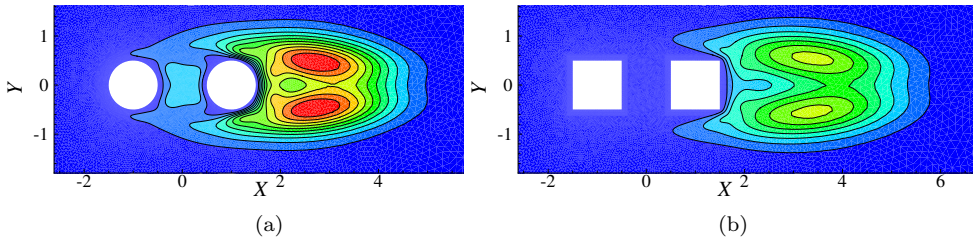


Fig. 14: Wavemaker region of (a) circular and (b) square cylinder at $(Re, L) = (60, 2D)$. The contour levels are from 0.04 to 0.35 in increments of 0.035 and the flow is from left to right.

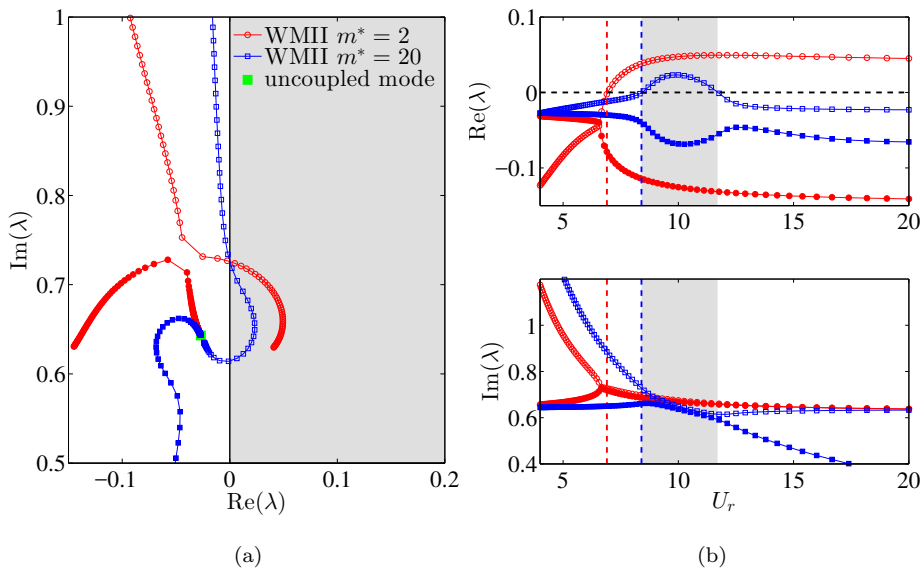


Fig. 15: Eigenspectrum of the ERA-based ROM at $(Re, L) = (60, 2D)$: (a) root loci as a function of the reduced velocity U_r , where the unstable right-half ($\text{Re}(\lambda) > 0$) plane is shaded in grey color. The WMI is denoted by filled symbols with the same shape as those for the WMII. The uncoupled wake mode $\lambda = -0.027 + 0.643i$. (b) Real and imaginary parts of the root loci at $(Re, L) = (60, 2D)$. The WIV region at $m^* = 20$ is shaded in grey colour, which is defined by $8.4 \leq U_r \leq 11.7$. - - - and - - - - represent WIV onset $U_r = 6.75$ and $U_r = 8.4$ for $m^* = (2, 20)$, respectively.

cylinder of a tandem pair. Journal of Fluid Mechanics **718**, 210245 (2013). DOI 10.1017/jfm.2012.606

2. ASSI, G.R.S., BEARMAN, P.W., MENEGHINI, J.R.: On the wake-induced vibration of tandem circular cylinders: the vortex interaction excitation mechanism. Journal of Fluid Mechanics **661**, 365401 (2010). DOI 10.1017/S0022112010003095
3. Bearman, P.W.: Circular cylinder wakes and vortex-induced vibrations. Journal of Fluids and Structures **27**(5), 648–658 (2011)

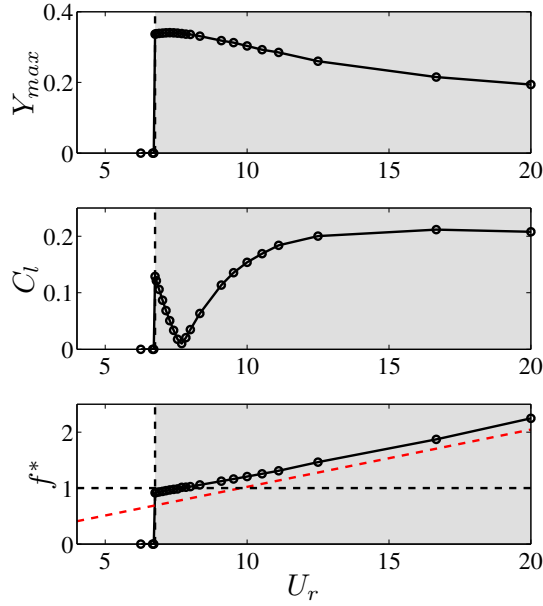


Fig. 16: Normalized maximum amplitude Y_{max} and rms value of lift coefficient C_l as a function of reduced velocity U_r at $(L, Re, m^*) = (2D, 60, 2)$. The WIV region is shaded in grey colour. - - - represents WIV onset $U_r = 6.76$. - - - - is the uncoupled WM frequency predicted by ROM.

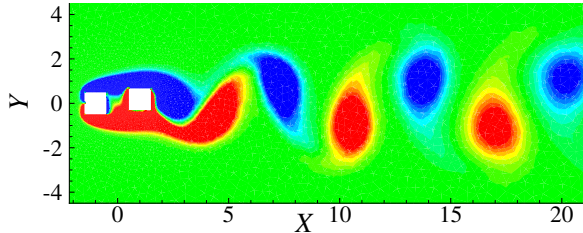


Fig. 17: Instantaneous vorticity contours of WIV onset ($U_r = 6.76$) at $(L, Re, m^*) = (2D, 60, 2)$. The contour levels are from 0.5 to 0.5 in increments of 0.067 and the flow is from left to right.

4. Bokaian, A., Geoola, F.: Wake-induced galloping of two interfering circular cylinders. *Journal of Fluid Mechanics* **146**, 383–415 (1984). DOI 10.1017/S0022112084001920
5. Giannetti, F., Luchini, P.: Structural sensitivity of the first instability of the cylinder wake. *Journal of Fluid Mechanics* **581**, 167–197 (2007)
6. Igarashi, T.: Characteristics of the flow around two circular cylinders arranged in tandem : 1st report. *Bulletin of JSME* **24**(188), 323–331 (1981). DOI 10.1299/jsme1958.24.323
7. Jaiman, R.K., Geubelle, P., Loth, E., Jiao, X.: Transient fluid-structure interaction with non-matching spatial and temporal discretizations. *Computers and Fluids* **50**, 120–135 (2011)

8. Juang, J.N., Pappa, R.S.: An Eigensystem Realization Algorithm for Modal Parameter Identification and Model Reduction. *J. Guidance* **8**(5), 620–627 (1985)
9. Mysa, R., Law, Y., Jaiman, R.: Interaction dynamics of upstream vortex with vibrating tandem circular cylinder at subcritical reynolds number. *Journal of Fluids and Structures* **75**, 27 – 44 (2017). DOI <https://doi.org/10.1016/j.jfluidstructs.2017.08.001>. URL <http://www.sciencedirect.com/science/article/pii/S0889974616303929>
10. Mysa, R.C., Kaboudian, A., Jaiman, R.K.: On the origin of wake-induced vibration in two tandem circular cylinders at low Reynolds number. *Journal of Fluids and Structures* **61**, 76–98 (2016)
11. Sarpkaya, T.: A critical review of the intrinsic nature of vortex-induced vibrations. *Journal of Fluids and Structures* **19**(4), 389–447 (2004)
12. Williamson, C.H.K., Govardhan, R.: Vortex-induced vibrations. *Annual Review of Fluid Mechanics* **36**, 413–455 (2004)
13. Yao, W., Jaiman, R.K.: Feedback control of unstable flow and vortex-induced vibration using the eigensystem realization algorithm. *Journal of Fluid Mechanics* **827**, 394414 (2017). DOI <10.1017/jfm.2017.470>
14. Yao, W., Jaiman, R.K.: Model reduction and mechanism for the vortex-induced vibrations of bluff bodies. *Journal of Fluid Mechanics* **827**, 357393 (2017). DOI <10.1017/jfm.2017.525>
15. Zdravkovich, M.: The effects of interference between circular cylinders in cross flow. *Journal of Fluids and Structures* **1**(2), 239 – 261 (1987)